ChemPubSoc Europe

DOI: 10.1002/chem.201903403

CHEMISTRY
A European Journal
Full Paper

Perovskite Phases

Defective $[Bi_2O_2]^{2+}$ Layers Exhibiting Ultrabroad Near-Infrared Luminescence

Hong Li[+],[a] Xiao-Fang Jia[+],[b] Qing Zhao[+],[c] Ju-Ping Ma,[a] Jian-Dang Liu,[d] Bang-Jiao Ye,[d] Yoshihiro Kuroiwa,[c] Chikako Moriyoshi,[c] Zhi-Yong Li,[a] Qi Liu,[a] Jun-Ying Zhang,*[b] and Hong-Tao Sun*[a]

Abstract: Aurivillius phases have been routinely known as excellent ferroelectrics and have rarely been deemed as materials that luminesce in the near-infrared (NIR) region. Herein, it is shown that the Aurivillius phases can demonstrate broadband NIR luminescence that covers telecommunication and biological optical windows. Experimental characterization of the model system $Bi_{2.14}Sr_{0.75}Ta_2O_{9-x}$, combined with theoretical calculations, help to establish that the NIR luminescence originates from defective $[Bi_2O_2]^{2+}$ layers. Importantly, the generality of this finding is validated based on observations of a rich bank of NIR luminescence characteristics in other Aurivillius phases. This work highlights that incorporating defects into infinitely repeating $[Bi_2O_2]^{2+}$ layers can be used as a powerful tool to space-selectively impart unusual luminescence emitters to Aurivillius-phase ferroelectrics, which not only offers an optical probe for the examination of defect states in ferroelectrics, but also provides possibilities for coupling of the ferroelectric property with NIR luminescence.

Introduction

The ability to control a variety of functions with external stimuli is at the heart of modern materials science.[1] In this pursuit, the incorporation of intrinsic or extrinsic atomic defects in structures that either exhibit naturally occurring vacancies or those with synthetically or postsynthetically introduced vacancies has been established as a powerful approach to the fine-tuning of the properties of a wide range of functional materials. Many of today's prominent materials, such as high-transition-temperature superconductors,[2,3] solar-driven photocatalysts,[4–7] photovoltaic materials,[8] metal–organic frameworks,[9–11] and ferroelectrics,[12–14] are imperfect systems with defect-induced, locally broken periodic structures, in which imperfection plays a pivotal role in governing, or at least affecting, their physiochemical properties.[15–20]

Materials consisting of a sequence of infinitely repeating stacks of $[Bi_2O_2]^{2+}$ layers, such as bismuth-based cuprate superconductors, bismuth oxyhalides, and Aurivillius phases, have attracted intensive attention because they exhibit an array of tantalizing properties, such as superconductivity, photocatalytic, photoluminescence (PL), and ferroelectricity.[4–7,12–14,21,22] In recent years, it has been shown that the macroscopic physiochemical properties of these materials are closely linked to their defect states. For instance, Zeljkovic et al. showed that nanoscale spatial variations in the pseudogap states in $Bi_{2+y}Sr_{2-y}CaCu_2O_{8+x}$ are particularly correlated with the presence of apical oxygen vacancies.[3] Additionally, defect engineering of materials with $[Bi_2O_2]^{2+}$ layers can make them superior to the corresponding defect-free counterparts for some targeted applications. It has been shown that the intentional introduction of defects into BiOCl nanosheets can significantly promote solar-driven photocatalytic activity, even with an extremely low photocatalyst loading.[4] These advancements thus spur great interest in utilizing defect chemistry for the discovery of new physical or chemical properties in materials with $[Bi_2O_2]^{2+}$ layers to maximize their potential. One of the most attractive features of bismuth-containing materials lies in the near-infrared (NIR) luminescence in the telecommunication and biological optical windows.[23–25] However, $[Bi_2O_2]^{2+}$ layers have rarely been deemed to be active in NIR luminescence. Given that incorporating atomic point defects in $[Bi_2O_2]^{2+}$ layers can break the local periodicity and affect the electronic structure of the

[a] H. Li,[+] J.-P. Ma, Z.-Y. Li, Q. Liu, Prof. Dr. H.-T. Sun
College of Chemistry, Chemical Engineering and Materials Science
Soochow University, Suzhou 215123 (P.R. China)
E-mail: timothyhsun@gmail.com

[b] X.-F. Jia,[+] Prof. Dr. J.-Y. Zhang
Key Laboratory of Micro-nano Measurement, Manipulation and Physics (Ministry of Education), School of Physics
Beihang University, Beijing 100191 (P.R. China)
E-mail: zjy@buaa.edu.cn

[c] Q. Zhao,[+] Prof. Dr. Y. Kuroiwa, Prof. Dr. C. Moriyoshi
Department of Physical Science, Hiroshima University
Higashihiroshima, Hiroshima 739-8526, (Japan)

[d] Dr. J.-D. Liu, Prof. Dr. B.-J. Ye
State Key Laboratory of Particle Detection and Electronics Department of Modern Physics
University of Science and Technology of China
Hefei, Anhui 230026 (P.R. China)

[+] These authors contributed equally to this work.

Supporting information and the ORCID identification number(s) for the author(s) of this article can be found under: https://doi.org/10.1002/chem.201903403.

crystalline lattice, we therefore hypothesized that this could offer chances to impart NIR luminescence to these materials, which would potentially provide new platforms to couple ferroelectricity with unusual photophysical properties.

Herein, we report on the discovery of ultrabroad NIR luminescence in defective Aurivillius phases that have been routinely known as excellent ferroelectrics. By taking $Bi_{2.14}Sr_{0.75}Ta_2O_{9-x}$ as a prototypical model system, we show that the Aurivillius structure can luminesce over an ultrabroad spectral range of $\lambda = 720$–1500 nm. Experimental characterization, including high-resolution synchrotron X-ray diffraction (SXRD), AFM, PL spectroscopy, and positron annihilation lifetime spectroscopy (PALS), combined with theoretical calculations, help us establish that the unconventional NIR luminescence originates from the defective $[Bi_2O_2]^{2+}$ layers. We propose a concept of the spatial separation of constituting structural units (i.e., chemically separating different luminescence emitters in one structure) for an in-depth understanding of the NIR PL mechanism, which has never been tried in the field of NIR-luminescent, bismuth-bearing photonic materials. Crucially, the generality of this finding is validated by the observation of a rich variety of NIR luminescence characteristics in other Aurivillius phases, including $Bi_{2-x}SrTa_2O_{9-y}$, $Bi_{2-x}CaTa_2O_{9-y}$, and $Bi_{4-x}Ti_3O_{12-y}$. Our work highlights the important role of defects located in $[Bi_2O_2]^{2+}$ layers in endowing Aurivillius ferroelectrics with ultrabroad luminescence properties, which provides a new avenue for further coupling of the ferroelectric property with NIR luminescence.

Results and Discussion

The layered perovskite, with a nominal composition of $Bi_{2.2}Sr_{0.8}Ta_2O_9$, was prepared by using a solid-state reaction method to yield micrometer-sized powders (Figure S1 in the Supporting Information). Elemental analysis through inductively coupled plasma atomic emission spectrometry (ICP-AES) gives a Bi/Sr/Ta molar ratio of 2.14:0.75:2.00. The XRD pattern can be well assigned to the orthorhombic phase with the space group of $A2_1am$, which confirms that the sample is a single phase (Figure S2 in the Supporting Information). To glean more structural information, Rietveld refinement of the high-resolution SXRD data was conducted by utilizing the general structure analysis system (GSAS) program (Figure 1 a).[26] The structure and corresponding refinement result are shown in Figure 1 b and Table S1 in the Supporting Information. Owing to the presence of more Bi and fewer Sr atoms in $Bi_{2.2}Sr_{0.8}Ta_2O_9$, compared with $Bi_2SrTa_2O_9$, partial Bi atoms occupy the crystallographic site of Sr; thus forming a disordered Aurivillius structure. Upon maintaining the occupancies of oxygen atoms as unity, while refining the occupancies of Sr and Bi atoms, introducing cation disorder at the Sr/Bi1 site leads to a satisfactory reliability factor ($R_{wp} = 3.34\,\%$, $\chi^2 = 5.55$) with reasonable isotropic displacement factors for all atoms; this yields a chemical composition of $Bi_{2.1413}Sr_{0.7538}Ta_2O_9$. Notably, the refined composition is almost identical to that obtained from ICP-AES, which strongly signifies the off-stoichiometry of the product. We surmise that this may be due to the evaporation of reactants at high temperatures. Considering all of this information, we took $Bi_{2.14}Sr_{0.75}Ta_2O_9$ as the composition, which can also be written as $[Bi_{1.95}O_2][Bi_{0.19}Sr_{0.75}Ta_2O_7]$.

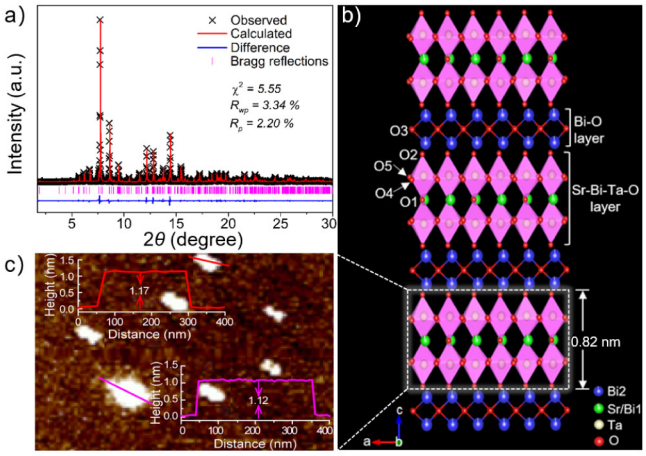

Figure 1. a) Rietveld fit to the high-resolution SXRD pattern of $Bi_{2.14}Sr_{0.75}Ta_2O_9$. b) Structure of $Bi_{2.14}Sr_{0.75}Ta_2O_9$. c) AFM image of the perovskite nanosheets. Insets show the corresponding height profiles of marked nanosheets.

We next separated different Bi atoms in $Bi_{2.14}Sr_{0.75}Ta_2O_9$ through a soft chemical exfoliation reaction,[27] yielding perovskite nanosheets as a result of the removal of $Bi_{1.95}O_2$ layers (see details in the Experimental Section). The TEM image of the exfoliated product clearly shows irregular sheet-like morphology, with a lateral size larger than 300 nm (Figure S3 in the Supporting Information). The AFM height profiles indicate that the nanosheets are of an average thickness of about 1.1 nm, which corresponds to the thickness of a perovskite-like monolayer in $Bi_{2.14}Sr_{0.75}Ta_2O_9$ (Figure 1 c). These results indicate successful exfoliation of layered $Bi_{2.14}Sr_{0.75}Ta_2O_9$ to monolayer nanosheets. No characteristic peaks of other phases and impurities are observed, which indicates the high purity of the nanosheets (Figure S2 in the Supporting Information). The molar ratio of Bi/Sr/Ta measured by means of ICP-AES is 0.20:0.74:2.00 for the nanosheets; this further confirms the disorder feature of the Sr/Bi1 site in $Bi_{2.14}Sr_{0.75}Ta_2O_9$. Interestingly, the absorption edge blueshifts from $\lambda = 368$ nm for $Bi_{2.14}Sr_{0.75}Ta_2O_9$ to $\lambda = 356$ nm for the nanosheets (Figure S4 a in the Supporting Information). The band gaps of $Bi_{2.14}Sr_{0.75}Ta_2O_9$ and nanosheets were determined to be 3.56 and 3.76 eV, respectively, based on the analysis of the diffuse-reflectance absorption spectra (Figure S4 b in the Supporting Information). This can be attributed to structural changes in the perovskite layer before and after exfoliation, as suggested by the XRD and Raman spectra (Figures S2 and S5 in the Supporting Information).

The aforementioned experimental results suggest that the obtained Aurivillius phase contains atomic point defects and that chemical exfoliation provides the possibility of decoupling the photophysical behavior of Bi atoms at the $Bi_{1.95}O_2$ and perovskite layers. As plotted in Figure 2 a, $Bi_{2.14}Sr_{0.75}Ta_2O_9$ shows a visible PL band at $\lambda = 525$ nm with two characteristic excitation bands at $\lambda = 304$ and 344 nm, whereas the nanosheets display a blueshifted PL at $\lambda = 510$ nm with an excitation maximum at

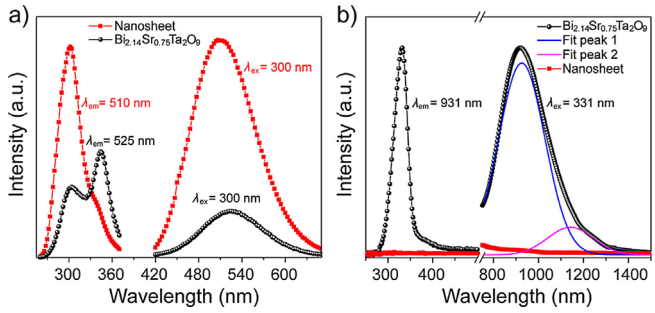

Figure 2. a) Visible PL and PL excitation spectra of $Bi_{2.14}Sr_{0.75}Ta_2O_9$ and the perovskite nanosheets. b) NIR PL and PL excitation spectra of $Bi_{2.14}Sr_{0.75}Ta_2O_9$ and nanosheets. The PL spectrum of $Bi_{2.14}Sr_{0.75}Ta_2O_9$ was decomposed into two Gaussian peaks, as indicated by blue and pink lines.

$\lambda = 302$ nm and an excitation shoulder at $\lambda = 339$ nm. Notably, the visible PL from both $Bi_{2.14}Sr_{0.75}Ta_2O_9$ and nanosheets are akin to those from Bi^{3+}-doped materials; this can be attributed to the electronic transition of $^3P_0 \rightarrow {}^1S_0$ under excitations corresponding to $^1S_0 \rightarrow {}^3P_1$ and $^1S_0 \rightarrow {}^3P_2$ transitions.[23,28] The blueshift of PL, as observed for the nanosheets, is in good agreement with the blueshift of the absorption bands, which we thus ascribe to the structural changes that occur in the perovskite layer (Figures S4 and S5 in the Supporting Information). Interestingly, close inspection of the photophysical properties in the NIR region reveal that $Bi_{2.14}Sr_{0.75}Ta_2O_9$ exhibits ultrabroad PL ranging from $\lambda = 720$ to 1500 nm, with an excitation maximum at $\lambda = 331$ nm and a long excitation tail from $\lambda = 360$ to 550 nm, which, however, is absent in the perovskite nanosheets (Figure 2b). The line shape of the NIR emission is asymmetric and can be decomposed into two emission bands at $\lambda = 926$ and 1142 nm after Gaussian fitting. Notably, a narrow NIR PL is observed in $Na_{0.5}Er_{0.5}Bi_4Ti_4O_{15}$; this stems from the electronic transition of Er^{3+} ions.[22] We emphasize that our finding represents an advance in work concerning the observation of ultrabroad NIR PL in ferroelectric Aurivillius phases, and thus, greatly enriches the bank of Bi-bearing NIR-luminescent materials.[23] On the basis of all structural and spectroscopic results, we conclude that the unconventional NIR emission stems from the defective $[Bi_{1.95}O_2]$ layer, whereas the visible PL is from the perovskite layer.

We sought to explore further why the defective $[Bi_{1.95}O_2]$ layer could show NIR PL through accurate examination of the defect states. PALS is a powerful technique to study defects in solids, and measuring the lifetime of the positron can offer information on the type and relative concentration of defects or vacancies, even at the ppm level.[4,29] Figure 3a shows the measured positron lifetime spectrum of $Bi_{2.14}Sr_{0.75}Ta_2O_9$, of which the corresponding fitted lifetime parameters are summarized in Table 1. $Bi_{2.14}Sr_{0.75}Ta_2O_9$ exhibits three lifetime components, τ_1, τ_2, and τ_3, with relative intensities of I_1, I_2, and I_3, respectively. The relative intensities can quantify the relative abundance of different defects. The longest lifetime components ($\tau_3 =$ 1922 ps), with a negligible relative intensity ($I_3 = 0.6\%$), could be attributed to positrons annihilated in certain large voids of $Bi_{2.14}Sr_{0.75}Ta_2O_9$.[4] Based on the theoretically calculated positron lifetimes (Table 2), the shortest one ($\tau_1 = 188.8$ ps; Table 1) observed in the experimental positron lifetime spectrum can be assigned to positrons trapped at single isolated oxygen vacancies, $V_{O3}^{\bullet\bullet}$, whereas another component ($\tau_2 = 308.8$ ps) can be attributed to positrons trapped at Bi–O vacancy associates (Figure 3b).[4,29] Clearly, the $V_{O3}^{\bullet\bullet}$ and $V_{Bi2}'''V_{O3}^{\bullet\bullet}V_{Bi2}'''$ defects are predominant in $Bi_{2.14}Sr_{0.75}Ta_2O_9$. PALS analysis was further complemented by X-ray photoelectron spectroscopy (XPS). As shown in Figure S6 in the Supporting Information, three peaks at 529.9, 531.5, and 532.7 eV can be identified from the O 1s core-level spectrum of $Bi_{2.14}Sr_{0.75}Ta_2O_9$, which can be assigned to lattice oxygen with perfect coordination, oxygen atoms in the vicinity of an oxygen vacancy, and surface-adsorbed oxygen, respectively.[4,30,31] These results indicate the existence of oxygen vacancies in $Bi_{2.14}Sr_{0.75}Ta_2O_9$. Although thermogravimetric analysis in an oxidizing atmosphere can be used for the determination of oxygen stoichiometry in some oxygen-deficient systems,[17,18] it is difficult to apply it to oxygen- and cation-deficient $Bi_{2.14}Sr_{0.75}Ta_2O_9$ because the lack of cations cannot stabilize the introduced oxygen atoms. Therefore, herein, we merely term defective $Bi_{2.14}Sr_{0.75}Ta_2O_9$ as $Bi_{2.14}Sr_{0.75}Ta_2O_{9-x}$. Collectively, these analyses strongly indicate that defects in $Bi_{2.14}Sr_{0.75}Ta_2O_{9-x}$, predominantly in the forms of $V_{O3}^{\bullet\bullet}$ and $V_{Bi2}'''V_{O3}^{\bullet\bullet}V_{Bi2}'''$, concentrate in the $[Bi_{1.95}O_2]$ layer, which thus leads us to connect the observed NIR PL with these defects.

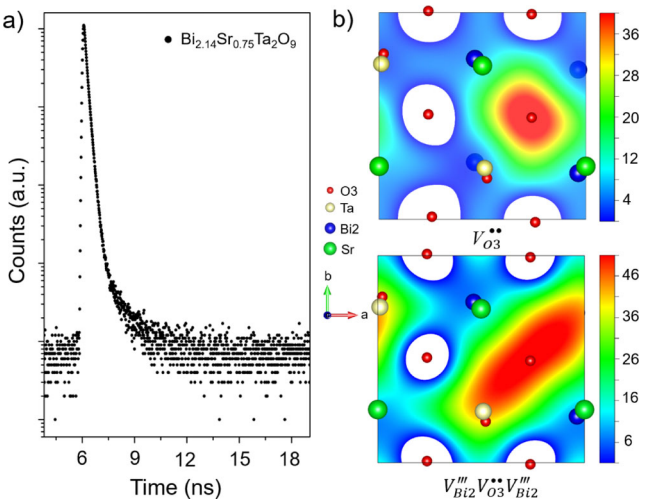

Figure 3. a) Positron lifetime spectrum of $Bi_{2.14}Sr_{0.75}Ta_2O_9$. b) Positron density in $Bi_{2.14}Sr_{0.75}Ta_2O_9$ along the (001) plane for trapped positrons in $V_{O3}^{\bullet\bullet}$ vacancies and $V_{Bi2}'''V_{O3}^{\bullet\bullet}V_{Bi2}'''$ vacancy associates.

Table 1. Positron lifetime parameters of $Bi_{2.14}Sr_{0.75}Ta_2O_9$.

Sample	τ_1 [ps]	τ_2 [ps]	τ_3 [ps]	I_1 [%]	I_2 [%]	I_3 [%]
$Bi_{2.14}Sr_{0.75}Ta_2O_9$	188.8	308.8	1922.0	34.9	64.5	0.6

Table 2. Calculated positron lifetimes of $Bi_{2.14}Sr_{0.75}Ta_2O_9$.

Defect	Bulk	$V_{O3}^{\bullet\bullet}$	$V_{Bi2}'''V_{O3}^{\bullet\bullet}V_{Bi2}'''$
lifetime [ps]	179.3	185.4	313.8

Importantly, we find that the NIR PL is not limited to $Bi_{2.14}Sr_{0.75}Ta_2O_{9-x}$, but also exists in other ferroelectric Aurivillius phases. For instance, $Bi_{2-x}SrTa_2O_{9-y}$ demonstrates similar a NIR PL to that of $Bi_{2.14}Sr_{0.75}Ta_2O_{9-x}$ under excitation at $\lambda = 332$ nm, whereas $Bi_{2-x}CaTa_2O_{9-y}$ displays a broad NIR emission at $\lambda =$ 810 nm under excitation at $\lambda = 376$ nm; $Bi_{4-x}Ti_3O_{12-y}$ has two NIR emission bands with maxima at $\lambda = 810$ and 1472 nm under excitation at $\lambda = 366$ nm (Figure S7 in the Supporting Information). We note that, akin to $Bi_{2.14}Sr_{0.75}Ta_2O_{9-x}$, these samples also possess oxygen vacancies (Figure S8 in the Supporting Information). All of these results suggest the generality of our findings.

To better understand the NIR PL mechanism, we then performed DFT calculations to establish the relationship between defect states and the observed PL behavior. Because $Bi_{2-x}SrTa_2O_{9-y}$ has a virtually identical PL to that of $Bi_{2.14}Sr_{0.75}Ta_2O_{9-x}$ (Figure S9 in the Supporting Information), we next calculated the band structure and the density of states (DOS) of $Bi_{2-x}SrTa_2O_{9-y}$ because of the computational cost to clarify the influence of defects on its electronic structure. The calculated band gap of pristine $Bi_2SrTa_2O_9$ is 2.6 eV (Figure S10 in the Supporting Information), which is smaller than that obtained experimentally.[32] Notably, the valence band maximum (VBM) is mainly composed of O 2p orbitals, whereas the conduction band minimum (CBM) consists mostly of Ta 5d orbitals. $V_{O3}^{\bullet\bullet}$ was confirmed to be the most stable oxygen vacancy by calculating the formation energies of the five systems containing oxygen vacancies (Table S2 in the Supporting Information); this is consistent with experimental results. The Bader charge estimates the nearby charges of an atom by calculating the charges that are enclosed within the Bader volume.[33] Figure 4 shows the amount of charges of all Bi atoms in $Bi_2SrTa_2O_9$, with serial numbers (nos. 1 to 32) labeled in Figure S11 in the Supporting Information. If oxygen vacancies exist in the $[Bi_{1.95}O_2]$ layers, four Bi atoms (nos. 2, 15, 20, and 21) around the vacancies gain electrons, resulting in the decreased valence state of Bi, as indicated by the calculated Bader charge of Bi atoms for perfect and deficient $Bi_2SrTa_2O_9$, with $V_{O3}^{\bullet\bullet}$ (Figure 4). This can be viewed as the occurrence of subvalent Bi in an undercoordinated geometry.[17] If $V_{Bi2}'''V_{O3}^{\bullet\bullet}V_{Bi2}'''$ defects exist in the $Bi_{1.95}O_2$ layers, the valence state of Bi around the vacancies does not notably change (Figure 4). We also tested the chemical states of Bi atoms using XPS; the results suggest the absence of Bi metallic atoms (Figure S12 in the Supporting Information). The band structure with $V_{O3}^{\bullet\bullet}$ oxygen vacancies does not change clearly (Figure 5a), but localized energy levels appear below the Fermi level (Figure 5b–f). Interestingly, the localized energy levels mainly

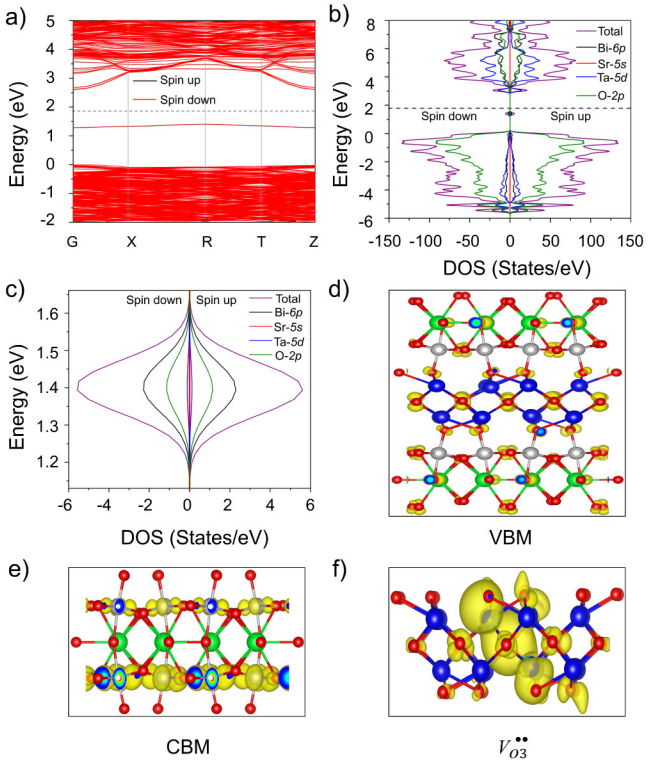

Figure 5. a) Band structure, b) DOS, and c) enlarged DOS of the mid-gap localized level of $Bi_2SrTa_2O_9$ with $V_{O3}^{\bullet\bullet}$, and partial densities of d) VBM and e) CBM, and f) the mid-gap localized level. Bi, blue; Sr, green; Ta, gray; and O, red.

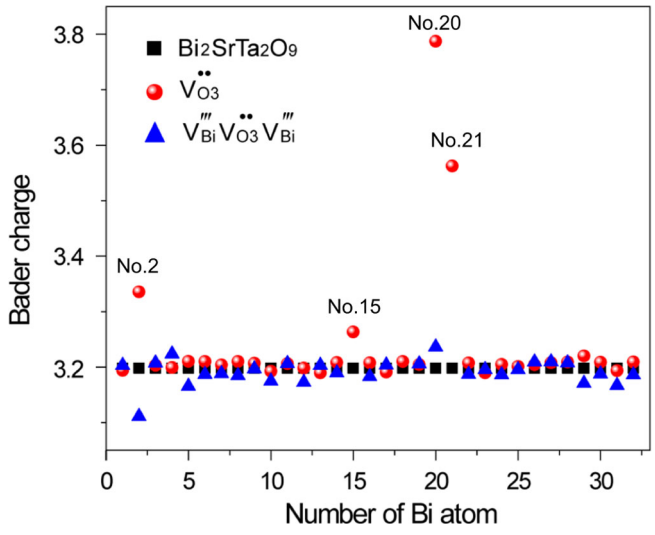

Figure 4. Bader charge of Bi atoms for perfect and deficient $Bi_2SrTa_2O_9$, with $V_{O3}^{\bullet\bullet}$ and $V_{Bi2}'''V_{O3}^{\bullet\bullet}V_{Bi2}'''$.

consist of Bi 6p and O 2p orbitals (Figure 5c). Under light excitation, in addition to charge transitions between VBM and CBM, there are also chances of charge transitions between this occupied mid-gap state and the CBM, which will result in the additional observed emission in the NIR region. If $V_{Bi2}'''V_{O3}^{\bullet\bullet}V_{Bi2}'''$ defects exist in the $Bi_{1.95}O_2$ layers, the band structure also does not change clearly (Figure 6a), and localized energy levels, mainly consisting of O 2p orbitals, appear (Figure 6b–f). The shallow empty localized energy levels located above the VBM can be thermally populated, and then charge transitions to the CBM can occur upon light excitation, which could also contribute to NIR emissions. If two kinds of defects coexist, the two groups of localized energy states could cause at least two series of emissions; this agrees well with the two experimental-

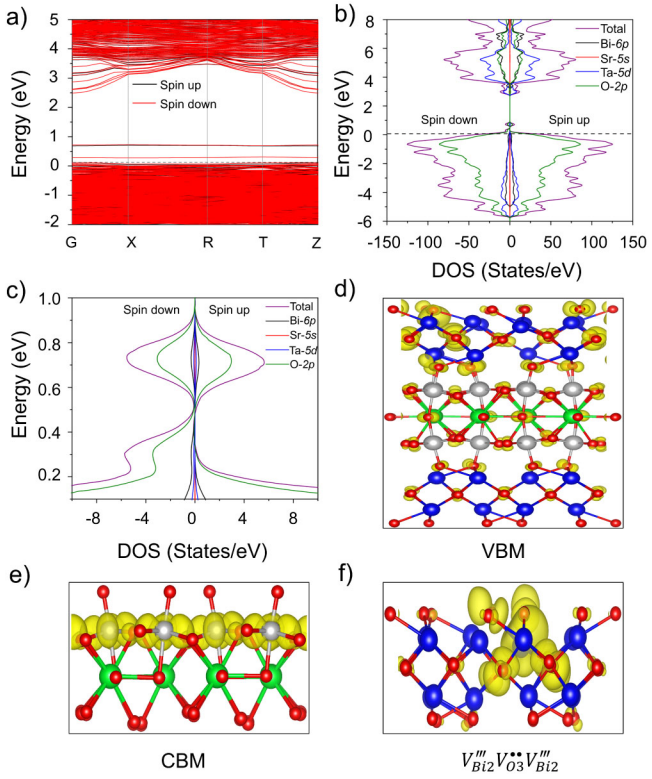

Figure 6. a) Band structure, b) DOS, and c) and enlarged DOS of the mid-gap localized level of $Bi_2SrTa_2O_9$ with $V'''_{Bi2}V^{\bullet\bullet\bullet}_{O3}V'''_{Bi2}$, and partial densities of d) VBM, e) CBM, and f) the mid-gap localized level. Bi, blue; Sr, green; Ta, gray; and O, red.

ly observed NIR emission bands (Figure 2b). The difference between the calculated and experimental results may result from the DFT method used in the calculation; this will not influence the prediction of the localized energy levels and the relative change of the band gap.[34,35]

Conclusion

We have demonstrated that conventional Aurivillius-phase ferroelectrics show ultrabroad NIR PL that covers the telecommunication and biological optical windows. A wide range of experimental and theoretical characterizations helped us to ascertain that the NIR luminescence originated from the defective $[Bi_2O_2]^{2+}$ layer. This allowed us to ask interesting questions about how the defect states could be fine-tuned in a well-controlled manner and how the ferroelectric and photophysical properties interacted with each other; this deserves to be further studied. It is also of interest to use the PL as a probe for the examination of defect states in ferroelectrics. We believe that the concept of spatial separation of constituting structural units demonstrated herein can be applied to the study of many Bi-containing luminescent materials, in particular, if more than one luminescent center coexists in one structure. We envisage that, as this family of $[Bi_2O_2]^{2+}$-layer-containing structures expands, defect engineering will enable us to discover many tantalizing physiochemical properties beyond those typically observed.

Experimental Section

Synthesis of $Bi_{2.2}Sr_{0.8}Ta_2O_9$

$Bi_{2.2}Sr_{0.8}Ta_2O_9$ powder was synthesized through a conventional solid-state method. Stoichiometric quantities of Bi_2O_3 (Aladdin, 99.99%), $SrCO_3$ (Aladdin, 99.95%), and Ta_2O_5 (Aladdin, 99.99%) powders were thoroughly ground to form a homogeneous fine powder as the starting compound. Mixtures were first calcined at 900 °C in air for 12 h. After cooling to room temperature naturally, the products were reground and subsequently sintered for 4 h at 1150 °C under a flow of pure oxygen (200 mL min^{-1}, >99.999%) to obtain the fully oxygenated powders. Afterwards, the products were slowly cooled to room temperature and white powders were collected.

Protonation of $Bi_{2.2}Sr_{0.8}Ta_2O_9$

The protonated powder was obtained through the acid treatment of $Bi_{2.2}Sr_{0.8}Ta_2O_9$. In detail, this process was carried out by stirring as-synthesized $Bi_{2.2}Sr_{0.8}Ta_2O_9$ (0.3 g) dispersed in a 3 M aqueous solution of HCl (100 mL) for 5 days at room temperature. The solution of HCl was replaced daily to ensure complete ion exchange. After the reaction, the obtained precursor was isolated through filtration and washed with distilled water several times to remove residual chloride ions. The as-prepared product was then dried at 80 °C for 12 h in a drying oven.

Exfoliation of the protonated powder

Exfoliation was typically performed by stirring the protonated powders (0.1 g) with a 0.1 M solution of ethylamine (10 mL) for 5 days at room temperature. The suspension was then centrifuged two times at 5000 rpm for 10 min to separate fully the sediment and supernatant solution, and the supernatant was used as the nanosheet solution.

Characterization

The composition of the samples was determined by ICP-AES (710-ES, Varian). Laboratory XRD data were obtained at room temperature by using a diffractometer (D2 PHASER, Bruker) with a $Cu_{K\alpha}$ radiation source ($\lambda = 1.5418$ Å). The high-resolution SXRD measurements were recorded on the BL02B2 beam line of SPring-8 to obtain high-quality diffraction patterns at room temperature. The samples for high-resolution SXRD were sealed into Hilgenberg glass capillaries with an inner diameter of 0.1 mm. The capillary was rotated during measurements to reduce the preferred orientation effect and average the intensity. The X-ray wavelength used was $\lambda = 0.4141$ Å. Rietveld structural refinements were performed against the XRD data by utilizing the GSAS program. Confocal Raman scattering measurements were carried out by using a micro-Raman spectrometer (Horiba Jobin Yvon, Labram HR 800) with a $\lambda = 532$ nm laser line and a power of 2 mW. XPS measurements were performed by using a Thermo Scientific ESCALAB 250Xi spectrometer, with an $AL_{K\alpha}$ source and 20 eV analyzer pass energy. Binding energies were corrected by the C 1s peak at 284.8 eV. The field-emission SEM images were obtained by using a Hitachi SU8010 scanning electron microscope. TEM images were collected from samples added to copper grids by using a FEI Tecnai G20 S-TWIN TMP microscope operating at an accelerating voltage of 200 kV. Tapping-mode AFM images of as-prepared nanosheets were measured by using a Multimode 8 microscope (Bruker, USA). Room-temperature diffuse-reflectance spectra were measured with a UV/Vis/NIR spectrophotometer (Cary 5000, Agilent)

equipped with an integrating sphere accessory. The obtained reflectance spectra were converted into pseudoabsorbance spectra by means of the Kubelka–Munk transformation. Room-temperature steady-state emission and excitation spectra were acquired by using an FLS 980 spectrofluorometer with a continuous (450 W) xenon lamp (Edinburgh Instruments).

Positron annihilation measurements

To detect structural defects in the as-prepared sample, positron annihilation spectrometry measurements were carried out with an ORTEC fast–fast coincidence system with a time resolution of about 200 ps in full-width at half-maximum (FWHM) at room temperature. The as-prepared sample was pressed into a round disk with a diameter of 8 mm and a thickness of 1 mm, and then a 20 μCi positron source of ^{22}Na was sandwiched between two identical samples. The total counts of each lifetime spectrum exceeded three million. Positron lifetime spectra were deconvoluted by using the LT9 code. One channel represents a time of 12.7 ps. Positron lifetime calculations were performed by using DFT together with the generalized gradient approximation (GGA), in which the positron densities were obtained in the self-consistent two-component DFT schemes. Models of 2×2×1 supercells were used for positron lifetime calculations of $Bi_{2.2}Sr_{0.8}Ta_2O_9$ with an unrelaxed structure vacancy. The crystal structure and electron-density distributions were drawn with the VESTA program.

DFT calculations

Spin-polarized DFT calculations were performed by using the Vienna ab initio simulation package (VASP) codes with the projector augmented wave (PAW) potentials.[36,37] We employed the Perdew–Burke–Ernzerhof (PBE) generalized gradient approximation (GGA) for the exchange-correlation function.[38] The cutoff energy for the plane-wave basis, the self-consistent total-energy difference, and the convergence criterion for forces on atoms were set to 500 eV, 10^{-4} eV, and 0.01 eV Å^{-1}, respectively. A Monkhorst–Pack grid of 5×5×1 was selected in the first Brillouin zone. In the band structure and DOS, the Fermi level of intrinsic $Bi_2SrTa_2O_9$ was set to zero. The energy shift for the Fermi levels of systems with defects were corrected by the average potential of Sr atoms far away from the defect site.

Acknowledgements

We are grateful for financial support from the National Natural Science Foundation of China (grant nos. 11874275, 11574225, and 51672106) and a project funded by the Priority Academic Program Development of Jiangsu Higher Education Institutions (PAPD). The SPring-8 experiments were carried out with the approval of the Japan Synchrotron Radiation Research Institute (JASRI; Proposal No. 2017B1309).

Conflict of interest

The authors declare no conflict of interest.

Keywords: Aurivillius phases · bismuth · luminescence · perovskite phases

[1] H. L. Tuller, S. R. Bishop, *Annu. Rev. Mater. Res.* **2011**, *41*, 369 – 398.
[2] H. Eisaki, N. Kaneko, D. L. Feng, A. Damascelli, P. K. Mang, K. M. Shen, Z. X. Shen, M. Greven, *Phys. Rev. B* **2004**, *69*, 064512.
[3] I. Zeljkovic, Z. Xu, J. Wen, G. Gu, R. S. Markiewicz, J. E. Hoffman, *Science* **2012**, *337*, 320 – 323.
[4] M. Guan, C. Xiao, J. Zhang, S. Fan, R. An, Q. Cheng, J. Xie, M. Zhou, B. Ye, Y. Xie, *J. Am. Chem. Soc.* **2013**, *135*, 10411 – 10417.
[5] F. Lei, Y. Sun, K. Liu, S. Gao, L. Liang, B. Pan, Y. Xie, *J. Am. Chem. Soc.* **2014**, *136*, 6826 – 6829.
[6] H. Li, J. Shang, Z. Ai, L. Zhang, *J. Am. Chem. Soc.* **2015**, *137*, 6393 – 6399.
[7] H. Wang, D. Yong, S. Chen, S. Jiang, X. Zhang, W. Shao, Q. Zhang, W. Yan, B. Pan, Y. Xie, *J. Am. Chem. Soc.* **2018**, *140*, 1760 – 1766.
[8] J. S. Park, S. Kim, Z. Xie, A. Walsh, *Nat. Rev. Mater.* **2018**, *3*, 194 – 210.
[9] T. D. Bennett, A. K. Cheetham, A. H. Fuchs, F. X. Coudert, *Nat. Chem.* **2016**, *9*, 11 – 16.
[10] S. Dissegna, K. Epp, W. R. Heinz, G. Kieslich, R. A. Fischer, *Adv. Mater.* **2018**, *30*, 1704501.
[11] S. Dissegna, P. Vervoorts, C. L. Hobday, T. Duren, D. Daisenberger, A. J. Smith, R. A. Fischer, G. Kieslich, *J. Am. Chem. Soc.* **2018**, *140*, 11581 – 11584.
[12] H. Higashijima, S. Kohiki, S. Takada, A. Shimizu, K. Yamada, *Appl. Phys. Lett.* **1999**, *75*, 3189 – 3191.
[13] B. H. Park, S. J. Hyun, S. D. Bu, T. W. Noh, J. Lee, H. D. Kim, T. H. Kim, W. Jo, *Appl. Phys. Lett.* **1999**, *74*, 1907 – 1909.
[14] J.-Y. Kim, I. Chung, J.-H. Choy, G.-S. Park, *Chem. Mater.* **2001**, *13*, 2759 – 2761.
[15] M. A. Hayward, M. A. Green, M. J. Rosseinsky, J. Sloan, *J. Am. Chem. Soc.* **1999**, *121*, 8843 – 8854.
[16] G. Kaur Behrh, H. Serier-Brault, S. Jobic, R. Gautier, *Angew. Chem. Int. Ed.* **2015**, *54*, 11501 – 11503; *Angew. Chem.* **2015**, *127*, 11663 – 11665.
[17] B. M. Liu, Z. G. Zhang, K. Zhang, Y. Kuroiwa, C. Moriyoshi, H. M. Yu, C. Li, L. R. Zheng, L. N. Li, G. Yang, Y. Zhou, Y. Z. Fang, J. S. Hou, Y. Matsushita, H.-T. Sun, *Angew. Chem. Int. Ed.* **2016**, *55*, 4967 – 4971; *Angew. Chem.* **2016**, *128*, 5051 – 5055.
[18] H. S. Kim, J. B. Cook, H. Lin, J. S. Ko, S. H. Tolbert, V. Ozolins, B. Dunn, *Nat. Mater.* **2017**, *16*, 454 – 460.
[19] T. Koketsu, J. Ma, B. J. Morgan, M. Body, C. Legein, W. Dachraoui, M. Giannini, A. Demortiere, M. Salanne, F. Dardoize, H. Groult, O. J. Borkiewicz, K. W. Chapman, P. Strasser, D. Dambournet, *Nat. Mater.* **2017**, *16*, 1142 – 1148.
[20] G. E. Wang, G. Xu, N. N. Zhang, M. S. Yao, M. S. Wang, G. C. Guo, *Angew. Chem. Int. Ed.* **2019**, *58*, 2692 – 2695; *Angew. Chem.* **2019**, *131*, 2718 – 2721.
[21] D. Kato, K. Hongo, R. Maezono, M. Higashi, H. Kunioku, M. Yabuuchi, H. Suzuki, H. Okajima, C. Zhong, K. Nakano, R. Abe, H. Kageyama, *J. Am. Chem. Soc.* **2017**, *139*, 18725 – 18731.
[22] X. Hui, D. Peng, H. Zou, J. Li, Q. Cao, Y. Li, X. Wang, X. Yao, *Ceram. Int.* **2014**, *40*, 12477 – 12483.
[23] H.-T. Sun, J. Zhou, J. Qiu, *Prog. Mater. Sci.* **2014**, *64*, 1 – 72, and references therein.
[24] B. Xu, S. Zhou, D. Tan, Z. Hong, J. Hao, J. Qiu, *J. Appl. Phys.* **2013**, *113*, 083503.
[25] H.-T. Sun, J. Yang, M. Fujii, Y. Sakka, Y. Zhu, T. Asahara, N. Shirahata, M. Ii, Z. Bai, J.-G. Li, H. Gao, *Small* **2011**, *7*, 199 – 203.
[26] A. C. Larson, R. B. Von Dreele, *Los Alamos National Laboratory Report LAUR 86 – 748*, **2000**.
[27] Y. Tsunoda, M. Shirata, W. Sugimoto, Z. Liu, O. Terasaki, K. Kuroda, Y. Sugahara, *Inorg. Chem.* **2001**, *40*, 5768 – 5771.
[28] S. Ida, C. Ogata, U. Unal, K. Izawa, T. Inoue, O. Altuntasoglu, Y. Matsumoto, *J. Am. Chem. Soc.* **2007**, *129*, 8956 – 8957.
[29] J. Li, X. Wu, W. Pan, G. Zhang, H. Chen, *Angew. Chem. Int. Ed.* **2018**, *57*, 491 – 495; *Angew. Chem.* **2018**, *130*, 500 – 504.
[30] E. McCafferty, J. P. Wightman, *Surf. Interface Anal.* **1998**, *26*, 549 – 564.
[31] K. Zhang, C.-G. Ma, J.-Y. Zhang, B.-M. Liu, Y. Zhou, S.-Q. Guo, J.-Y. Xu, J.-S. Hou, Y.-Z. Fang, L.-R. Zheng, H.-T. Sun, *Adv. Opt. Mater.* **2017**, *5*, 1700448.
[32] A. Shimizu, S. Takada, H. Shimooka, S. Takahashi, S. Kohiki, M. Arai, M. Oku, *Chem. Mater.* **2002**, *14*, 3971 – 3975.
[33] J. Luo, J. Lu, H. Zhao, Y. Dai, Q. Liu, J. Yang, X. Jiang, H. Xu, *Phys. Status Solidi B* **2014**, *251*, 1212 – 1218.

[34] J. P. Perdew, M. Levy, *Phys. Rev. Lett.* **1983**, *51*, 1884 – 1887.
[35] Y. Gai, J. Li, S. S. Li, J. B. Xia, S. H. Wei, *Phys. Rev. Lett.* **2009**, *102*, 036402.
[36] G. Kresse, J. Furthmüller, *Phys. Rev. B* **1996**, *54*, 11169 – 11186.
[37] G. Kresse, D. Joubert, *Phys. Rev. B* **1999**, *59*, 1758 – 1775.
[38] J. P. Perdew, K. Burke, M. Ernzerhof, *Phys. Rev. Lett.* **1996**, *77*, 3865 – 3868.

Manuscript received: July 26, 2019
Accepted manuscript online: August 2, 2019
Version of record online: ■■ ■■, 0000

FULL PAPER

Perovskite Phases

H. Li, X.-F. Jia, Q. Zhao, J.-P. Ma, J.-D. Liu, B.-J. Ye, Y. Kuroiwa, C. Moriyoshi, Z.-Y. Li, Q. Liu, J.-Y. Zhang, H.-T. Sun**

■■ – ■■

Defective $[Bi_2O_2]^{2+}$ Layers Exhibiting Ultrabroad Near-Infrared Luminescence

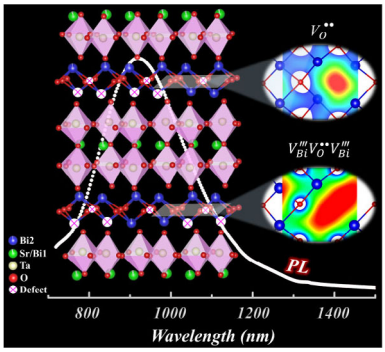

Beyond ferroelectricity: The defective $[Bi_2O_2]^{2+}$ layers in Aurivillius phases show broadband near-IR luminescence that covers the telecommunication and biological optical windows (see figure). The luminescence was identified to stem from oxygen vacancies and defect complexes. This offers a probe for the examination of defect states in Aurivillius-phase ferroelectrics and possibilities for coupling both physical behaviors.